1.1.1. Petrophysics Taken from the Narrative

Petrophysical analysis for 10 wells was completed using the Techlog* Wellbore Software Platform and the Quanti.Elan* multicomponent inversion solver to estimate porosity and permeability of the injection and confining zones targeted for carbon storage. Raw log data in both raster and LAS form were acquired from (IHS, 2019) and (DOGGR). The log basic log data were from wells drilled between 1942 and 1987 (Table 1). Logs were imported into the Techlog* software and normalized. Petrophysical properties such as effective porosity (PIGE), permeability (KINT) and volume of clay (VCL) were calculated and used to determine sand and shale facies. These properties were later used to populate the geologic model discussed in Section 1.1.2. Petrophysical results show a reasonable estimate of total porosity and permeability; however, there is uncertainty on the effective porosity because an empirical relationship was used to estimate irreducible water.

The petrophysical workflow involved building a model using well log data from NAPA AVE A/1 calibrated to core data for the same well (TGS, 2019). This workflow was applied to the other wells within the geologic model in which only well data was available to determine the porosity and permeability. As shown in Table 1, some of the wells have a limited set of well log data. The petrophysical property uncertainty around these wells was reduced by calibrating parameters and multi-well comparisons across different formations. The petrophysical evaluation focused on the formations included in the geological model from the Garzas formation to the Precambrian Basement. Petrophysical calculation results are illustrated in cross section Figure 1, Figure 2, Figure 3.

The minerology around the Mendota site is assumed to be like that from the well – NAPA AVE A/1 which is approximately 9 miles from the site and penetrates similar formations; however, there is uncertainty in the lateral continuity of the formations which could result in differences in the reservoir properties and minerology. This uncertainty will be significantly reduced by acquiring 3D seismic, logging a comprehensive suite of wireline tools and core data as detailed in (Schlumberger, Attachment G: Construction Details Clean Energy Systems Mendota, 2019) from a characterization well drilled in future phases of this project.

VCL logs derived from petrophysical modeling were used to generate a simple lithology log of sand and shale. VCL log values greater than 30% were considered shale and anything less than 30% VCL was flagged as sand. The resulting facies log is shown in Figure 1, Figure 2, Figure 3 cross sections. Facies definition will be re-evaluated and refined as new well data is added to the petrophysical model. Figure 4 shows facies thickness maps of the Moreno shale caprock and First and Second Panoche sand intervals. At Mendota_INJ_1, the estimated thickness of the First Panoche sand is 325 ft and the second Panoche sand 1000 ft. The Moreno shale caprock seal thickness is estimated at 1000 ft. Within the AoR the thickness of the injection target varies from approximately 1000-2000 ft. There are multiple overlaying shale formations. The Moreno shale main seal reaches thicknesses around 500-1700 ft, as show in Figure 4. Regional well data show Panoche sand targets to be continuous across the modeled area based on well log data as discussed in Section 2.2 and Section 2.4.2.

Table 1: Wells used to characterize petrophysical properties within the AoR

Well Name	UWI	Latitude (deg)	Longitude (deg)	Spud Date	Data Available[1]
AMBASSADOR NL & F/2	4039001440000	36.85492	-120.34239	09-23-1962	SP, DT and Resistivity
B B COMPANY /1	4019207520000	36.774431	-120.334662	04-12-1973	SP, DT and Resistivity
GILL / 38-16	4039000460000	36.79396	-120.23433	12-02-1942	SP and Resistivity
KERHY PROPERTIES / 1	4019216070000	36.86941	-120.21743	01-14-1978	GR, DT, RHOB, NPHI, Resistivity
NAPA AVE A /1	4019225380000	36.75919	-120.21387	01-24-1987	GR, DT, RHOB, NPHI, Resistivity and Core
NL & F ARNOLD / 1	4039200320000	36.86496	-120.39371	03-07-1982	SP, DT and Resistivity
SACHS MCNEAR NO 1_2	4019060420000	36.6767	-120.30546	08-18-1965	SP, DT and Resistivity
SALLABERRY / 1-6	4019215350000	36.74573	-120.26308	07-27-1981	GR, DT, RHOB, NPHI, Resistivity
STERLING COLEMAN /1	4019203700000	36.70535	-120.337582	07-14-1969	SP and Resistivity
YOUNG ETAL / 1	4019204110000	36.66817	-120.23627	12-19-1969	DT, RHOB, Resistivity

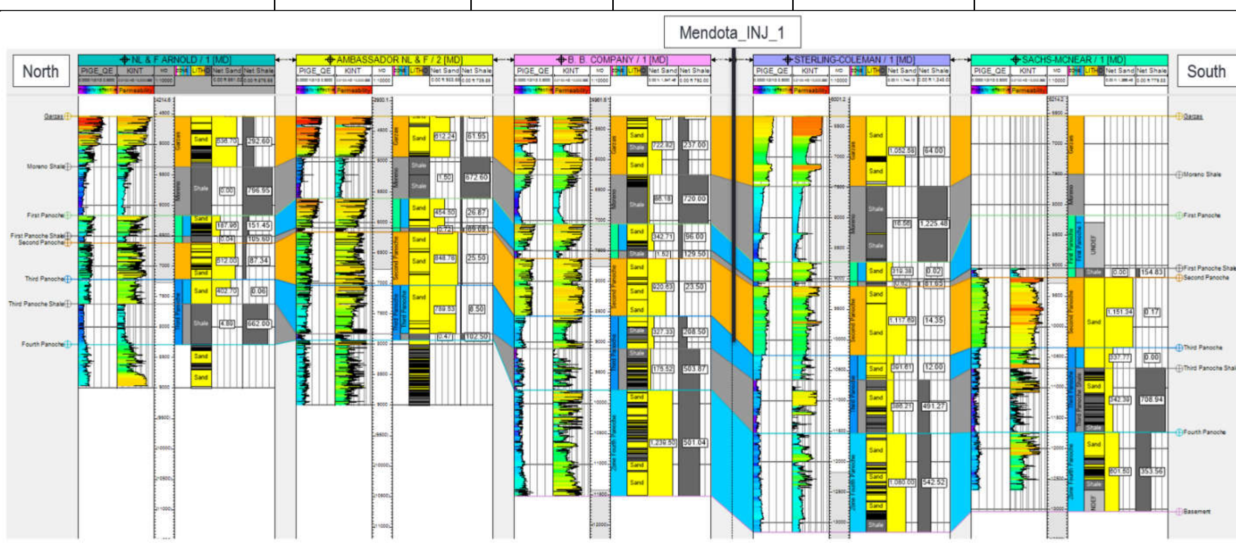

Figure 1: N-S Cross Section showing Petrophysical analysis results and wells nearest to Mendota_INJ_1. The tracks show left to right PIGE (Effective Porosity) KINT (Permeability), MD, Zone log, Sand and Shale Lithologies as calculated from VCL, and Net Lithology values for Sand and Shale per zone.

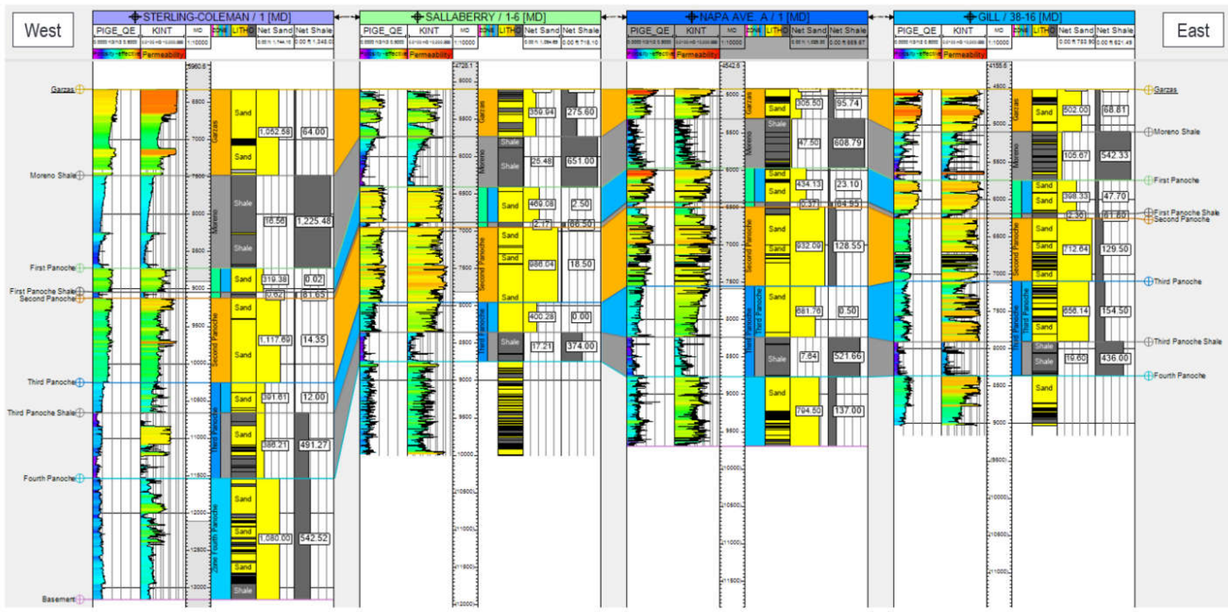

Figure 2: W-E Cross Section showing Petrophysical analysis results with same tracks as Figure 1.

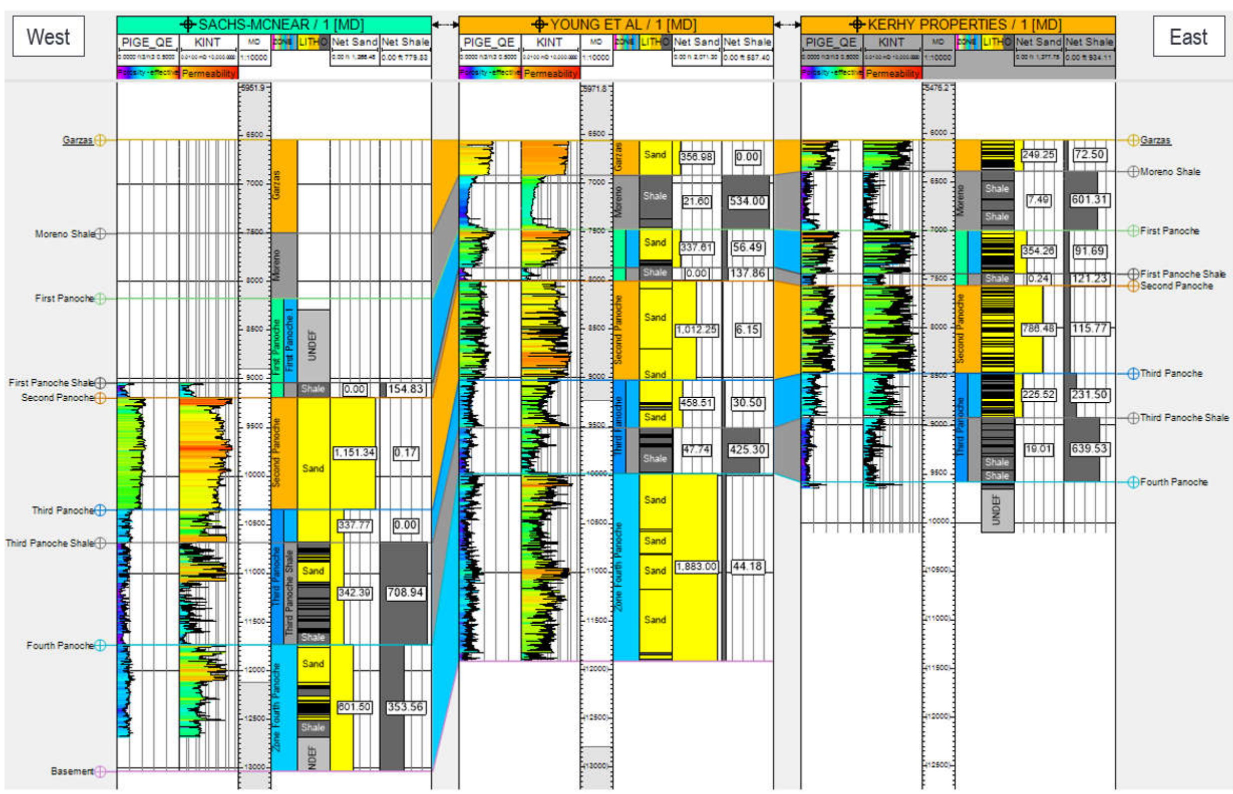

Figure 3: W-E 2 Cross section showing Petrophysical analysis results with same tracks as Figure 1.

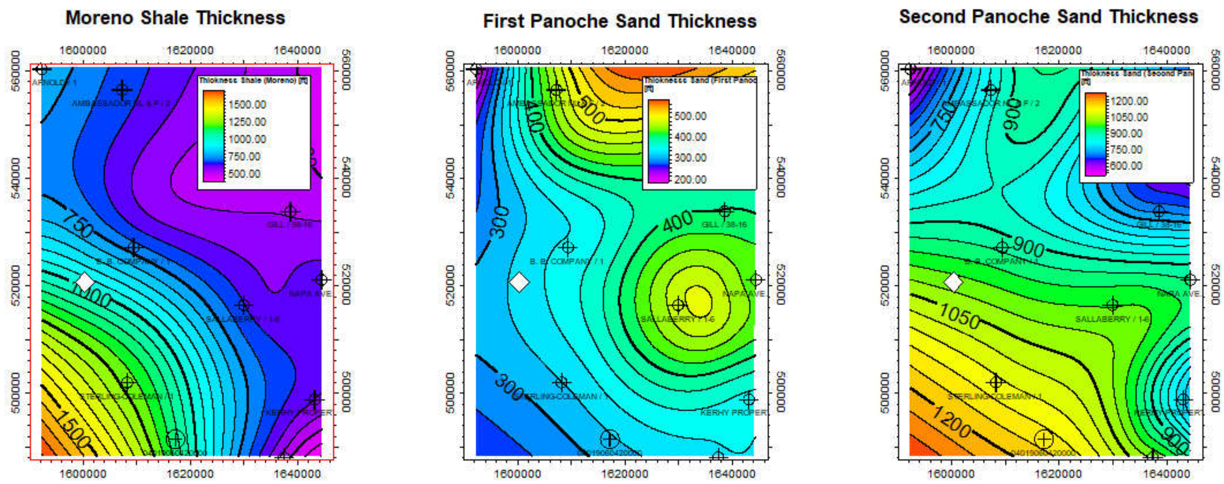

Figure 4: Net Thickness maps of Moreno Shale and First and Second Panoche Sands calculated based on VCL greater than or less than 30%, white diamond denotes Mendota_INJ_1.

1.1.1.1. Porosity

The total porosity of the injection zone was determined from either the bulk density or compressional slowness depending on data availability (Figure 5). The porosity of the Third and Fourth Panoche sands is lower than that of the First and Second Panoche sands as evident by the denser, faster log responses seen on the raw logs from all the wells within the geologic model. Clay volume was estimated from the spontaneous potential or gamma ray log to derive the clay bound water and with an empirical estimate of irreducible water gave an estimation of the effective porosity. This effective porosity was distributed into the geomodel. Figure 6 shows the spatial distribution of the effective porosity across both the injection and confining zones. The average effective porosity for the injection and confining zones is as shown in Table 2.

1.1.1.2. Permeability

The intrinsic permeability was estimated based on the porosity and lithology of the formation (Herron, 1987) using the wells around Mendota_INJ_1 (Figure 7). The lithology model consisted primarily of Quartz, Clay and Feldspars based on the core from NAPA AVE A/1. The relationship of porosity vs permeability is show in (Figure 8). The average permeability of both the injection and confining zones is shown in Table 2 and Figure 9 shows the spatial variations in permeability thickness (KH) for the different formations.

Table 2: Average porosity and permeability of injection and confining zones - average porosity and permeability of injection and confining zones

Formation	Average Porosity (%)	Average Permeability (mD)
Moreno Shale	8	4.7
First Panoche	20	300
Second Panoche	18	290
Third Panoche	12	140
Fourth Panoche	10	87

1.1.1.3. Mineralogy and Geochemistry Analysis

The minerology around the Mendota site is assumed to be similar to that from the well – NAPA AVE A/1. The core X-Ray Diffraction (XRD) report indicates the presence of Quartz, K-Feldspar, Plagioclase, Pyrite, Clay and Calcite stringers as shown in Table 3 (California Department of Conservation, 1998). Expected geochemical reactions to the injected CO_2 stream are discussed in the narrative. A more comprehensive analysis is planned using core and geochemical logs from a characterization well in a future phase of this project.

Table 3: Mineralogy summary from core XRD – NAPA AVE A 1

Depth	Quartz	K-Feldspar	Plagioclase	Calcite	Ankerite	Siderite	Pyrite	Barite	Clay
ft	%	%	%	%	%	%	%	%	%
8200	32	22	35				4		7
8208	15	10	22	1			7		45
8222	19	13	20				5	3	33
8612	36	20	33						9
8618	20	12	16	25	3	11			9
8751	36	20	33					1	10

1.1.2. Geocellular Modeling and Volumetrics

In order to estimate the spatial distribution of rock properties between wells, structural surfaces were used to build the skeleton for a 3D geocellular model. The lateral grid resolution (cell size) was defined as 400 ft by 400 ft. A finer resolution grid will be considered for future modeling after incorporation of 3D seismic data. The 3D model was divided into 4 ft layer increments, and log data from the 10 petrophysical wells was upscaled into the cells along the wellbore. The upscaled log data (discussed in section 1.1.1) provides the basis for populating the geomodel properties which include effective porosity, permeability, clay volume and pore volume. Petrophysical properties were distributed through the model domain using the Gaussian Random Function Simulation (GRFS) algorithm. This kriging based algorithm was used because it can generate multiple equiprobable realizations, which is preferred when working with sparse well data. Before running this simulation, it is necessary to define vertical, major and minor variograms to guide property distribution. Variogram modeling based on petrophysical logs shows a NE-SW depositional trend, with a vertical resolution of roughly 20 ft. 20 ft is likely representative of larger depositional changes (for example from high-stand to low-stand sea level). To capture smaller changes within each depositional cycle, 4 ft layer increments were defined for each zone. Because modeled zones are based on estimated facies changes, facies logs were not used as bias in the porosity or permeability models at this time. Facies biasing and Kriging to 3D seismic data will be considered in future model iterations.

Histograms for porosity and permeability comparing petrophysical logs to upscaled (averaged based on layer increment) and to full-field simulated properties are illustrated in Figure 5 and Figure 7. The relationship between porosity and permeability are shown in the Figure 8 cross plots. Once colored by zone and facies, the distributions show distinguishable separation; therefore, estimated porosity and permeability ranges can be predicted for the injection and confining zone. Figure 6 and Figure 9 show the simulated average porosity and simulated permeability thickness (KH) for each modeled zone is consistent with regional geology and predicted lithology type. The Moreno shale formation has low porosity and low permeability which is required to act as an effective seal. The Second Panoche injection zone has high porosity and permeability throughout the model domain area. Figure 10 shows a 2D view with Mendota_INJ_1 at the center and North-South, East-West transverses. This 3D view shows the confining and injection zone to be continuous within the model domain, and confining zones with low porosity are present above and below the Second Panoche target injection zone. Spatial distributions for porosity, permeability and clay volume are illustrated in Figure 11 through Figure 16.

The storage capacity of the injection zone was measured in bulk volume ft^3. The integrity of the confining zone is measured based on the thickness of Moreno shale and available core data. Within a 2.5-mile radius of the Mendota_INJ_1, the total pore volume of the Second Panoche injection zone is calculated using the 3D geocellular model; for each model cell, the porosity was multiplied by the cell volume. The total pore volume was calculated to be 3.74×10^{11} ft^3. Given the high porosity and permeability of the Second Panoche, this formation is suitable to receive the forecasted 350,000tons/year of CO_2.

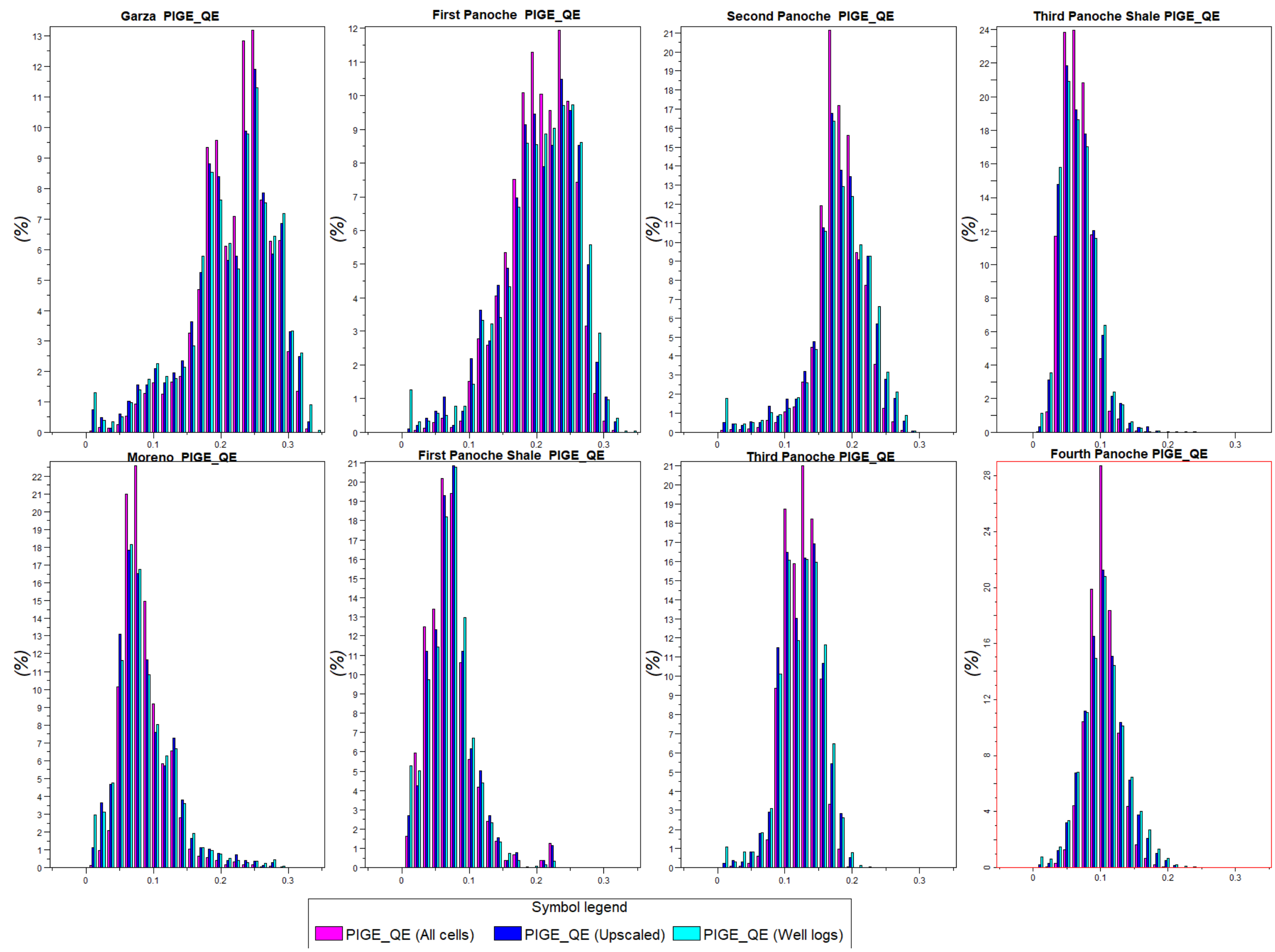

Figure 5: Porosity histograms of well logs, upscaled cells and model cells

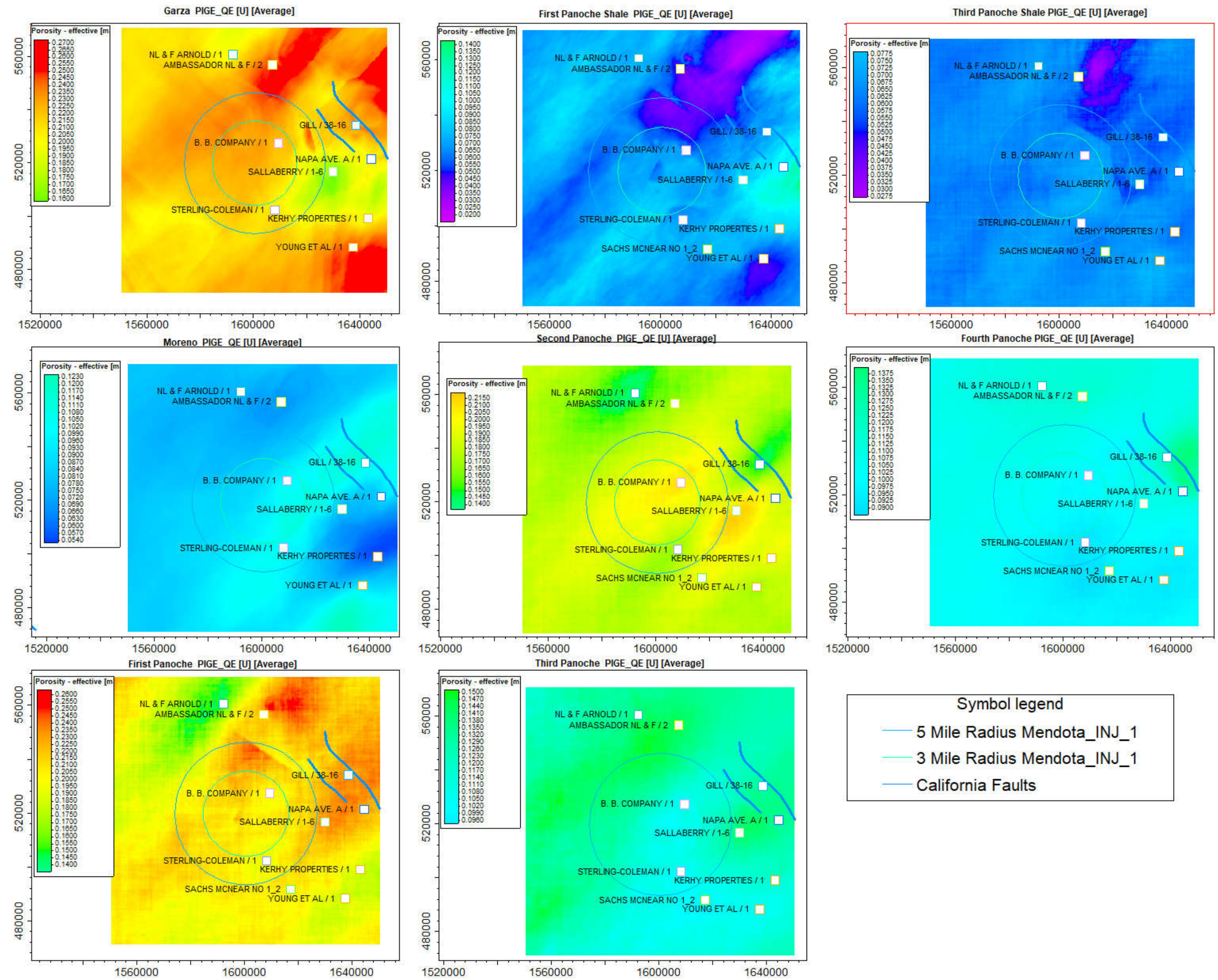

Figure 6: Modeled average porosity maps for each formation

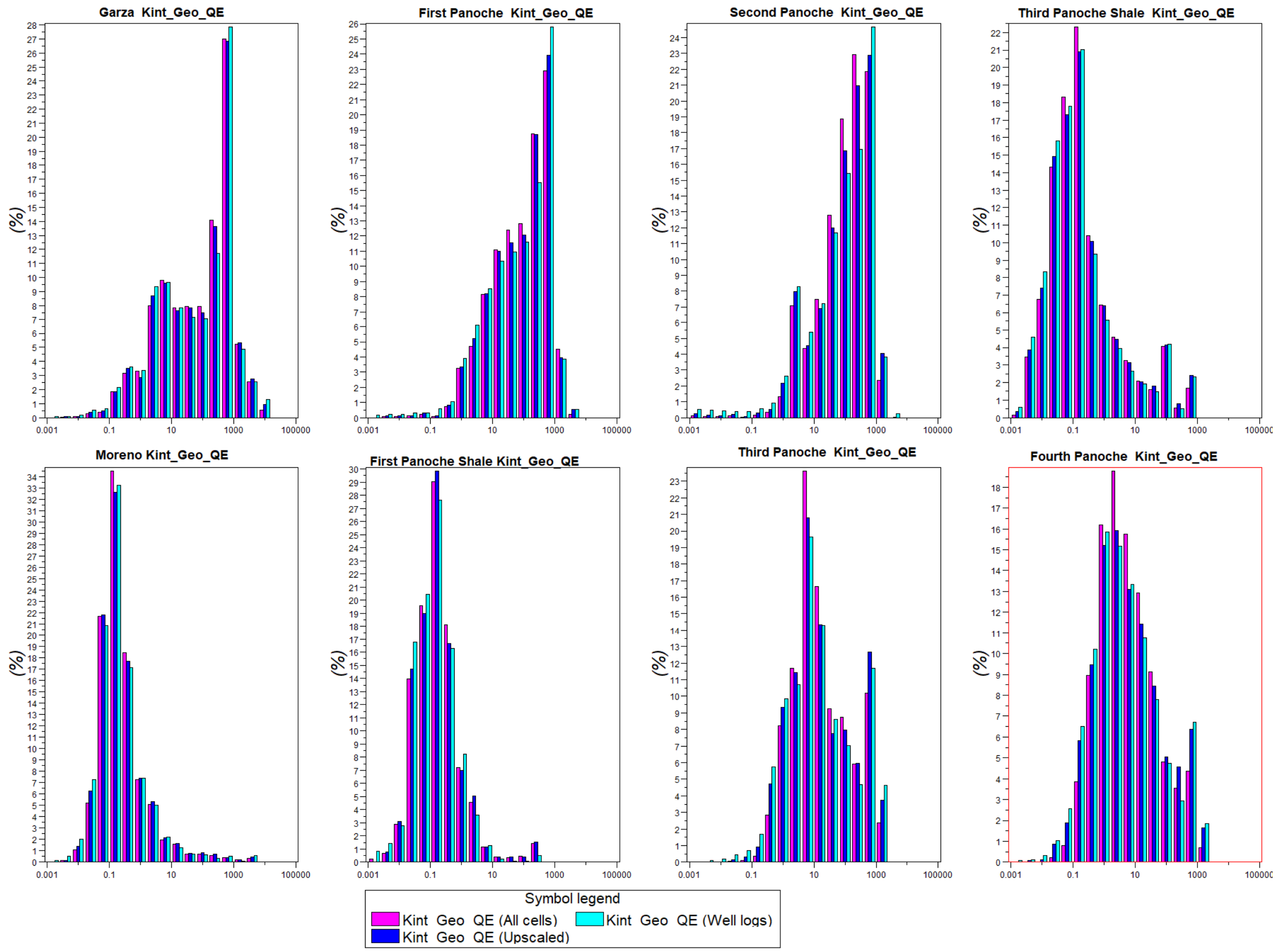

Figure 7: Permeability histograms of well logs, upscaled cells and model cells

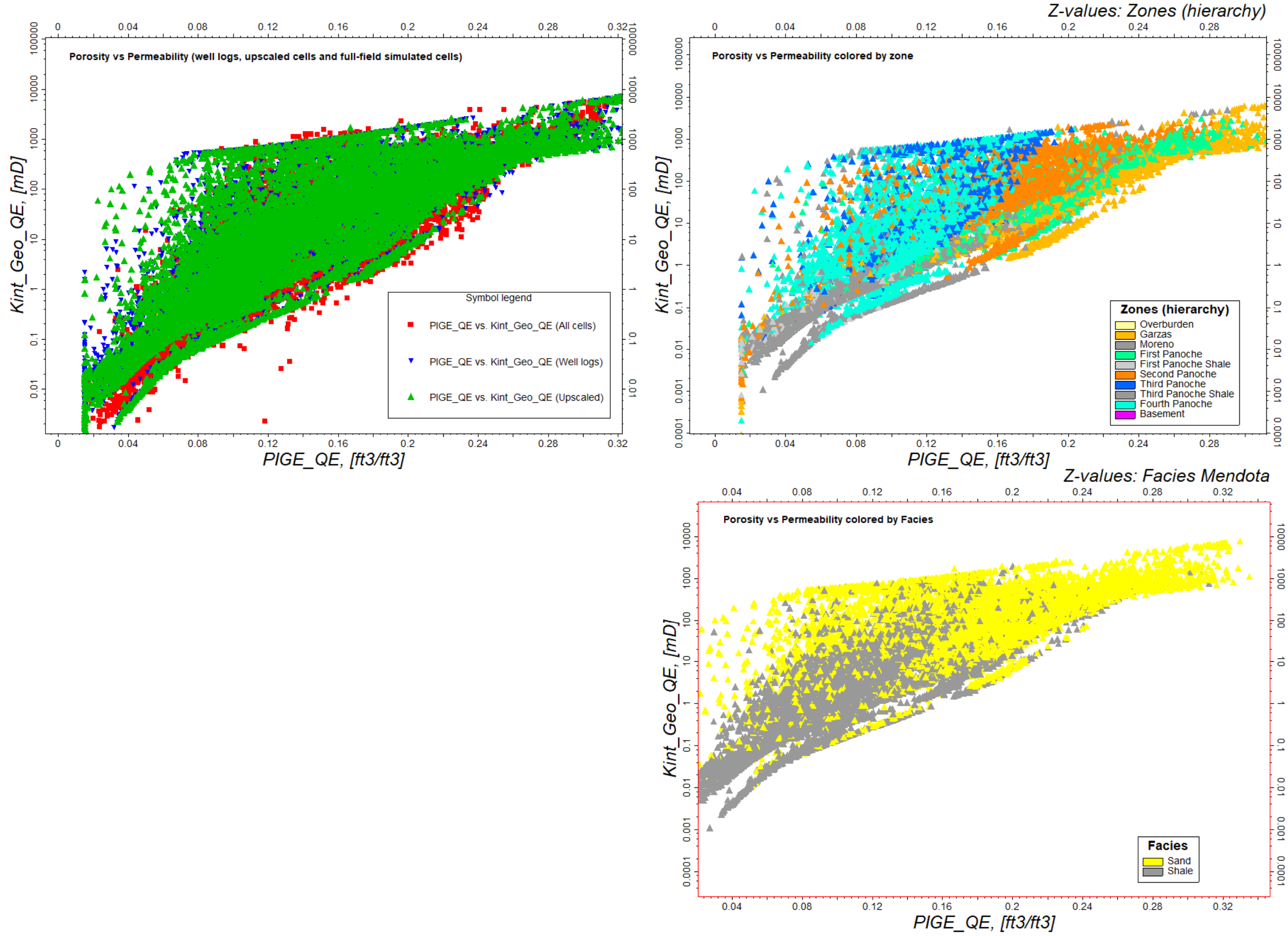

Figure 8:Porosity permeability cross plot of upscaled cells and model cells (left) and upscaled cells colored by formation

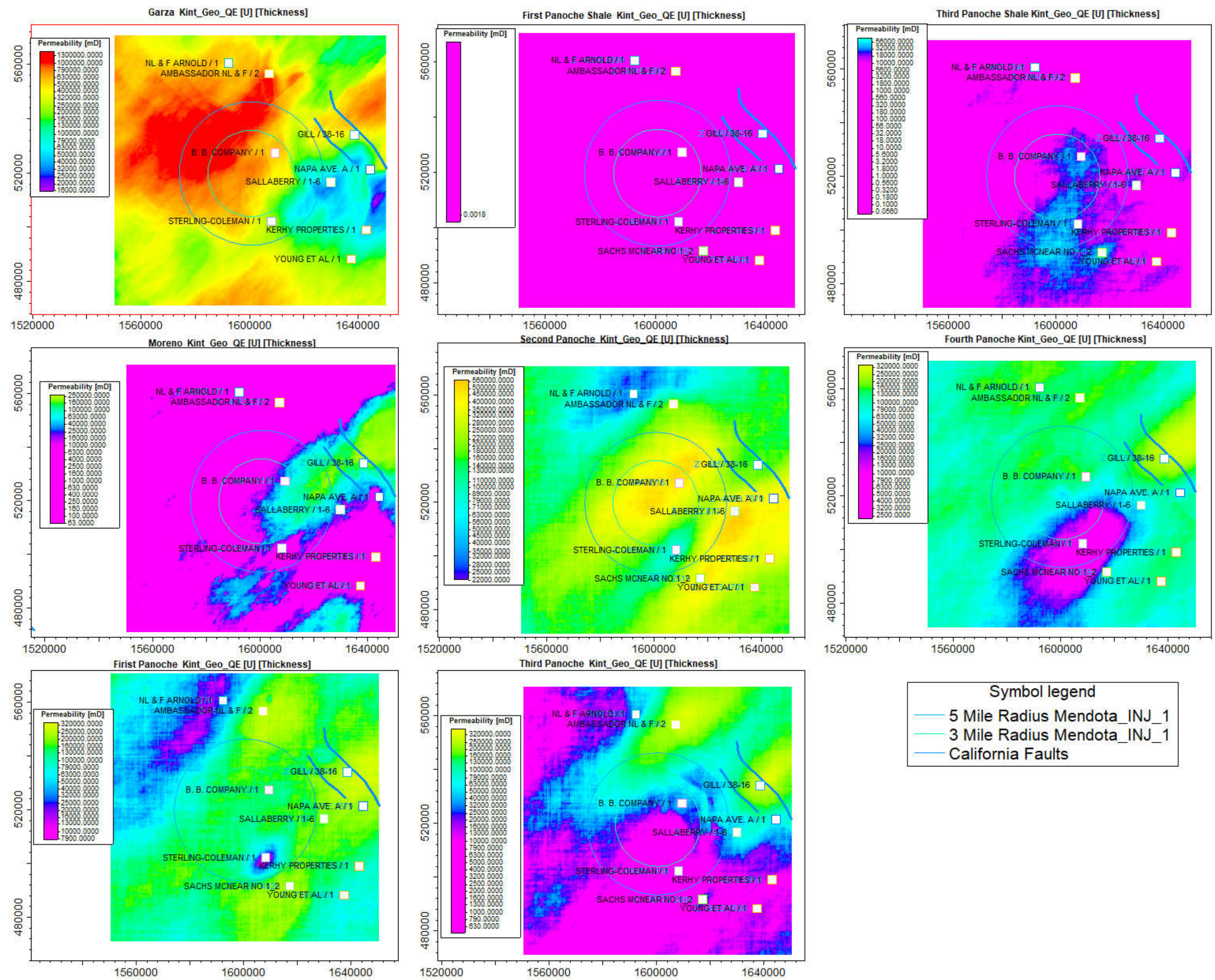

Figure 9: Modeled permeability thickness (KH) maps for each formation

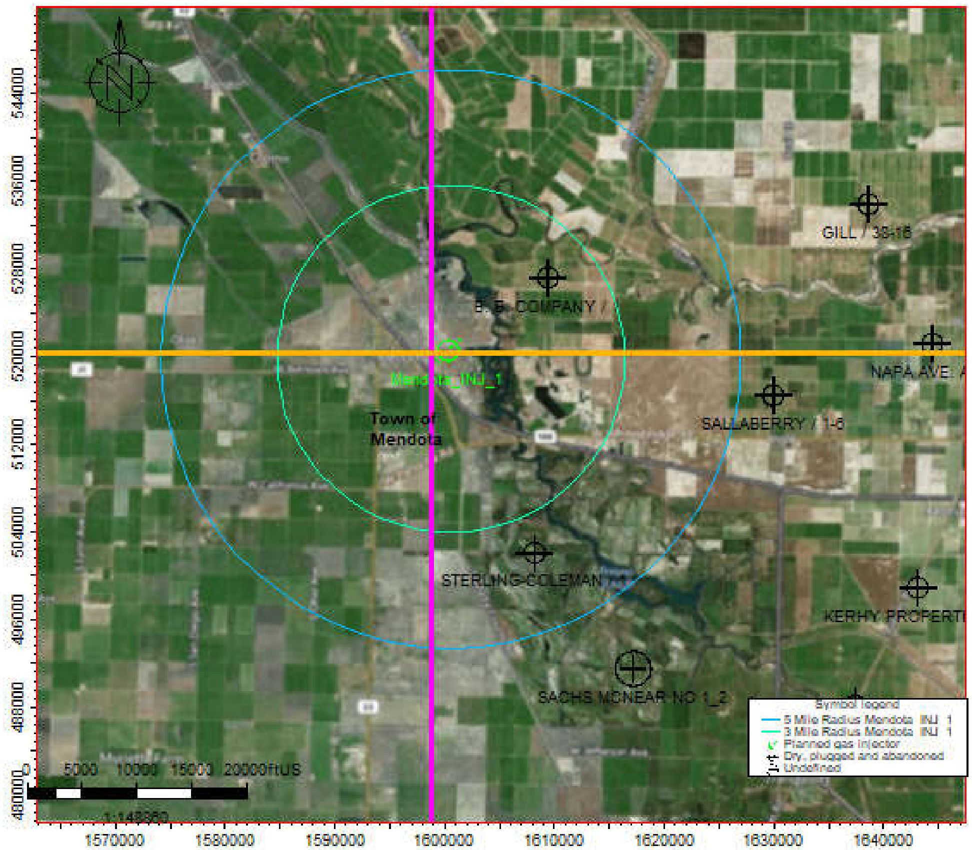

Figure 10: Injection well cross-section traverse map, N-S an E-W

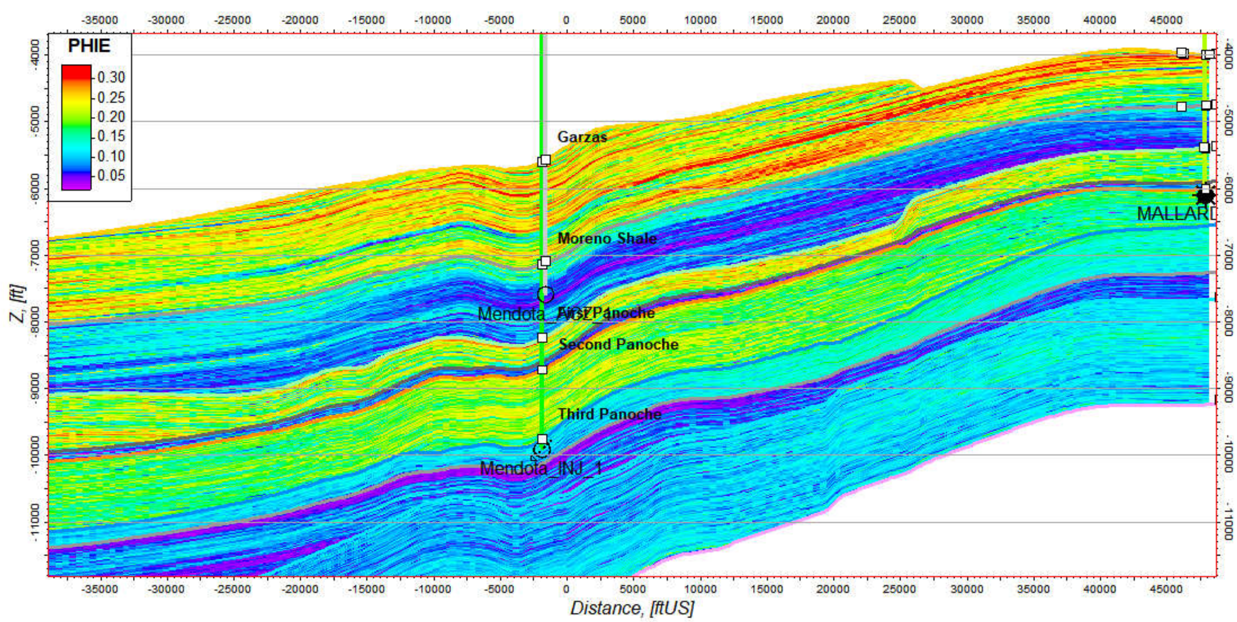

Figure 11: Effective Porosity Model Cross-section (N-S)

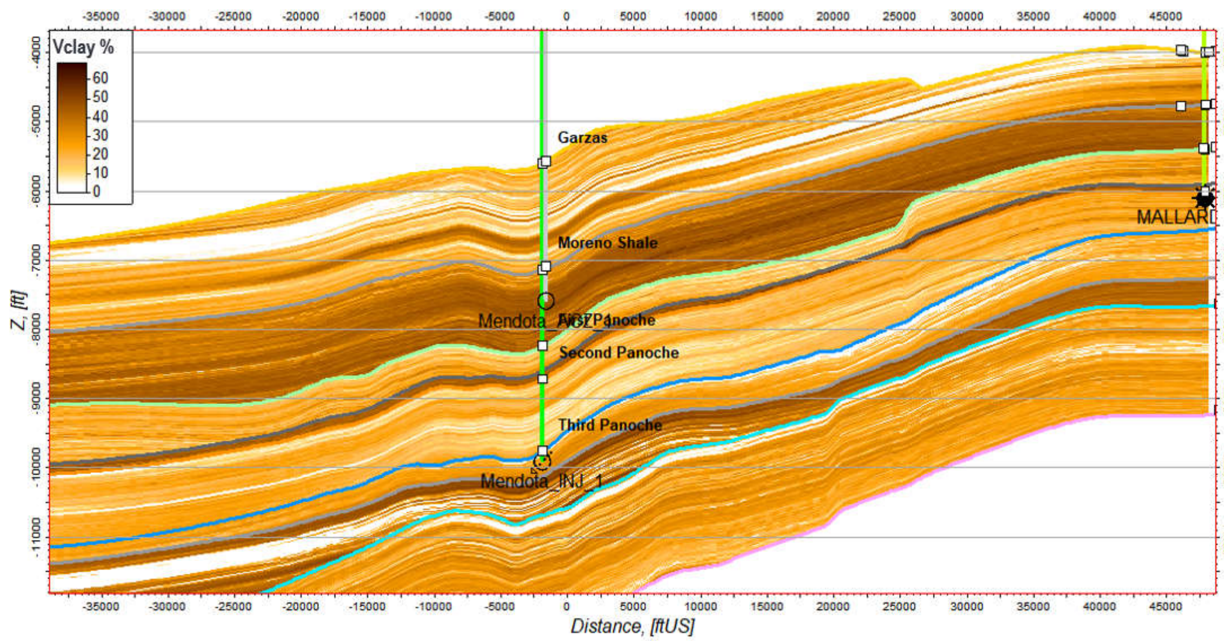

Figure 12: Volume clay model cross-section (N-S)

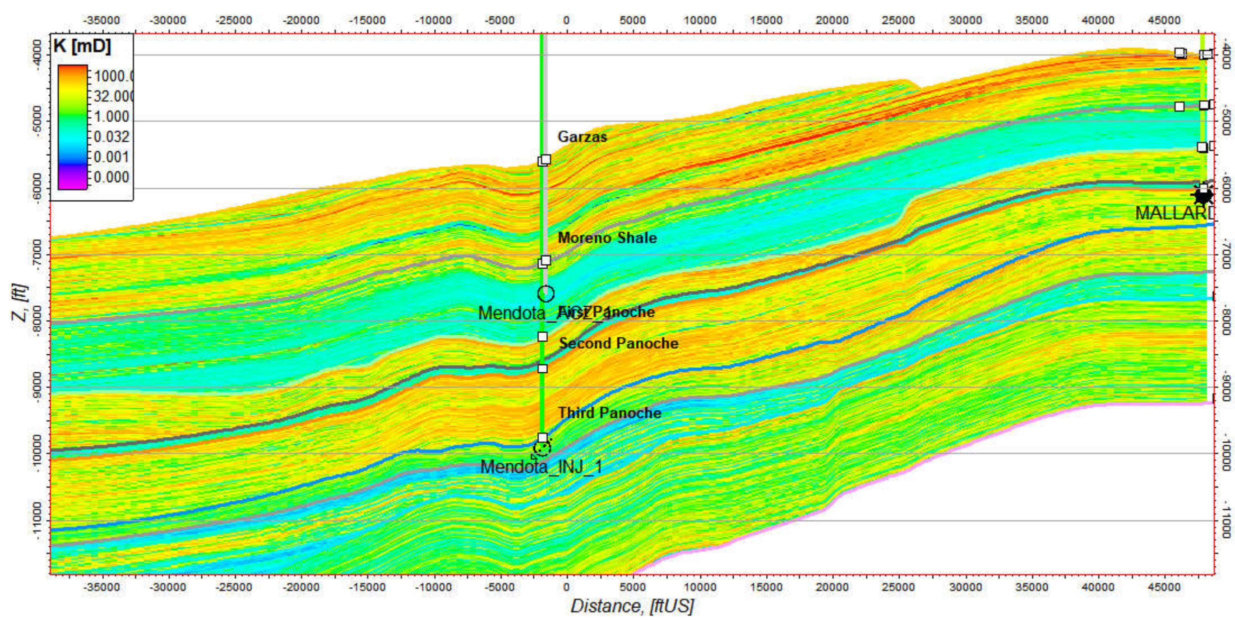

Figure 13: Permeability model cross-section (N-S)

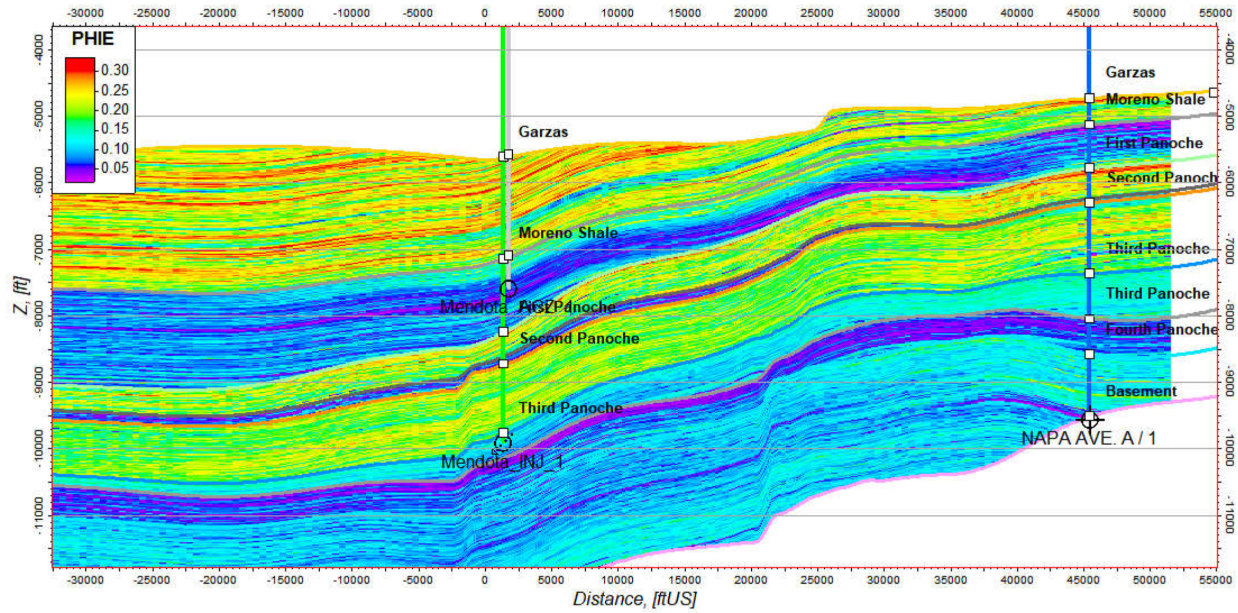

Figure 14: Effective porosity model cross-section (E-W)

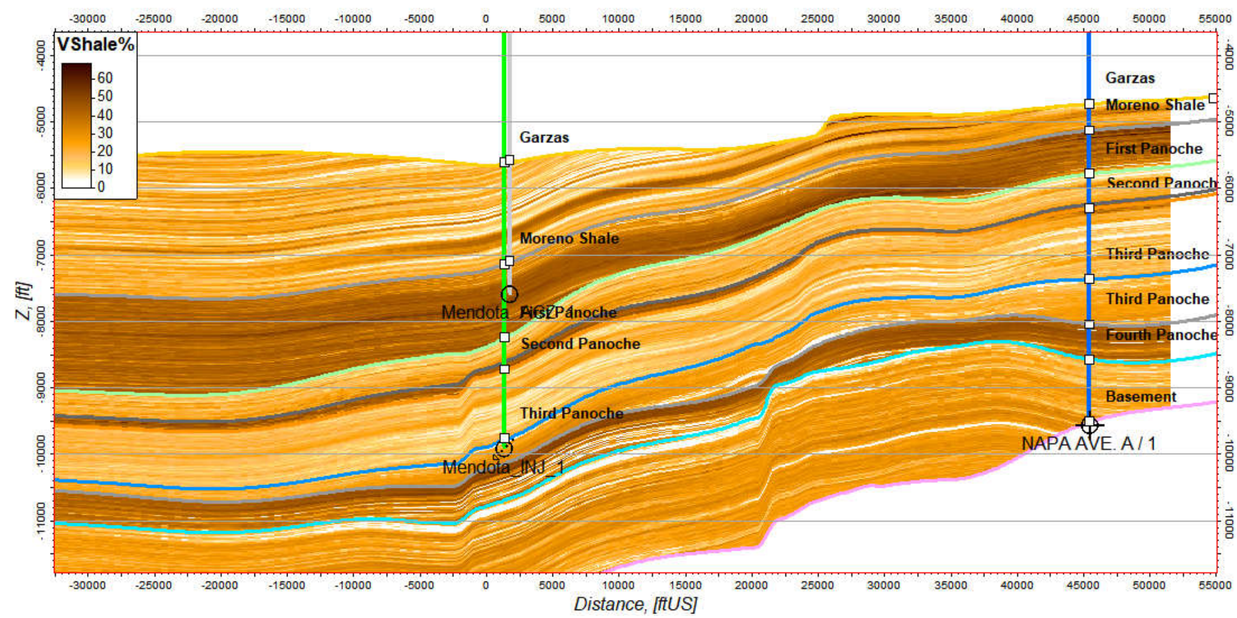

Figure 15: Volume Shale Model Cross-section (E-W)

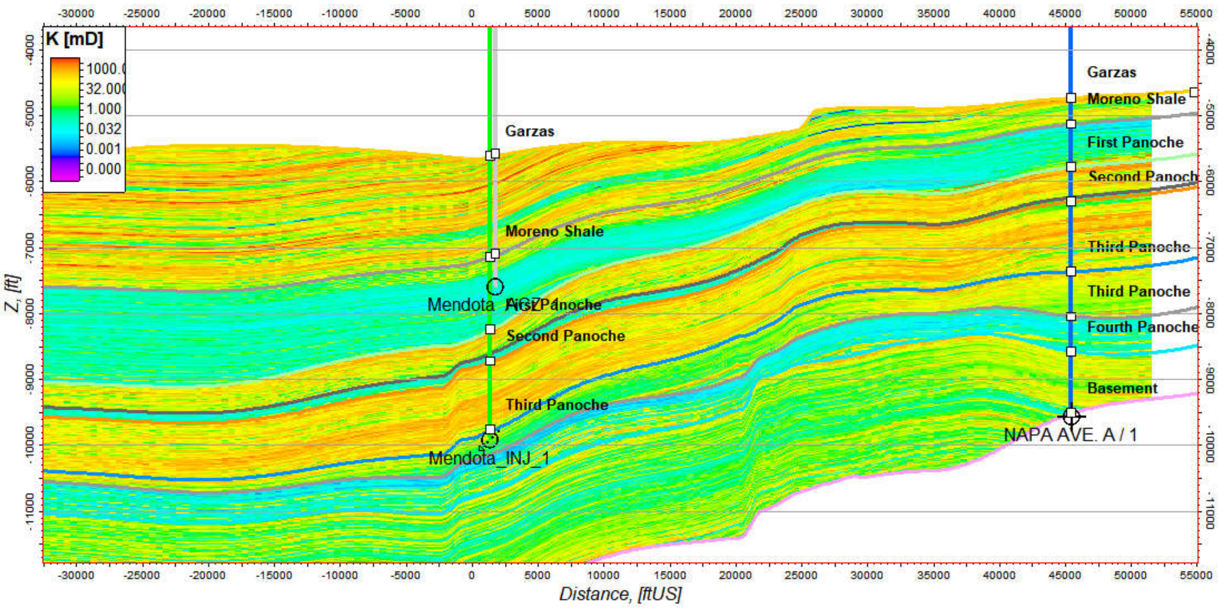

Figure 16: Permeability Model Cross-section (E-W)

2. References

Bartow, A. J. (1990). *1990 Bartow and Nilsen USGS Review of the Great Valley Sequence, eastern Diablo Range and northern San Joaquin Valley, central California.* USGS.

California Department of Conservation, D. o. (1998). *CALIFORNIA OIL & GAS FIELDS Volumes I, II, & III.*

California Department of Water Resources. (n.d.). Retrieved from water.ca.gov/Library/Other-DWR-Portals

CEMA. (2010). *Central Coast ShakeOut Area - Historical Epicenters*. Retrieved from https://www.shakeout.org/california/images/Central_Coast_epicenters_map.jpg

Chanchani, S. Z. (2003). A case study of hydrocarbon transport along active faults and production-related stress changes in the Monterey formation, California. *Geological Society, London, Special Publications*, 17-26.

Chiaramonte, L. Z. (2008). Seal integrity and feasibility of CO 2 sequestration in the Teapot Dome EOR pilot: Geomechanical site characterization. *Environmental Geology*, 1667-1675.

DOGGR. (2019). *https://www.conservation.ca.gov/dog*. Retrieved from Division of Oil, Gas, and Geothermal Resources.

EPA. (2018). *Geologic Sequestration of Carbon Dioxide Underground Injection Control (UIC) Program Class VI Implementation Manual for UIC Program Directors.*

EPA. (2019). *Class VI Guidance Documents*. Retrieved from Class VI Guidance Documents: https://www.epa.gov/uic/class-vi-guidance-documents

EPA. (2019). *Underground Injection Control* . Retrieved from https://www.epa.gov/uic/class-ii-permit-application-checklist

Gillespie, J. (2017). *Groundwater salinity in the southern San Joaquin Valley.* AAPG Bulletin, v. 101, no. 8 (August 2017), pp. 1239–1261.

Han, D. N. (1986). Effects of porosity and clay content on wave velocities in sandstone. *Geophysics*, 2093-2107.

Herron, M. M. (1987). Estimating the Intrinsic Permeability of Clastic Sediments from Geochemical Data. *SPWLA 28th Annual Logging Symposium.*

Herron, M. M. (June 29-July 2, 1987). Estimating the Intrinsic Permeability of Clastic Sediments from Geochemical Data. *SPWLA Twenty-Eighth Annual Logging Symposium*.

IHS. (2019). *IHS Markit*. Retrieved from Enerdeq, Lognet: https://ihsmarkit.com/index.html

McGuire, D. (1988). Depositional framework of the Upper Cretaceous-lower Tertiary Moreno Formation, central San Joaquin basin, California. *SPEM*.

Peng, D. Y., & Robinson, D. B. (1976). A New Two-Constant Equation of State. *Industrial and Engineering Chemistry: Fundamentals*, 15: 59–64.

Scheirer, A. H. (2003). Winters-Domengine Total Petroleum System - Northern Nonassociated Gas Assessment Unit of the San Joaquin Basin Providence. In U. S. Team, *Petroleum Systems and Geologic Assessment of Oil and Gas in the San Joaquin.*

Schlumberger Quality Assurance and Surveillance Plan. (2020). *Quality Assurance and Surveillance Plan.*

Schlumberger, Attachment A: Summary of Requirements Class VI Operating. (2020). *Attachment A: Summary of Requirements Class VI Operating and Reporting Conditions.*

Schlumberger, Attachment B: Area of Review and Corrective Action Plan. (2020). *Attachment B: Area of Review and Corrective Action Plan 40 CFR 146.84(b) Clean Energy Systems Mendota.*

Schlumberger, Attachment C: Testing and Monitoring Plan. (2020). *Attachment C: Testing and Monitoring Plan 40 CFR 146.90 Clean Energy Systems Mendota.*

Schlumberger, Attachment D: Injection Well Plugging Plan. (2020). *Attachment D: Injection Well Plugging Plan 40 CFR 146.92(B) Clean Energy Systems Mendota.*

Schlumberger, Attachment E: Post-Injection Site Care and Site Closure Plan. (2020). *Attachment E: Post-Injection Site Care and Site Closure Plan 40 CFR 146.93(A) Clean Energy Systems Mendota.*

Schlumberger, Attachment F: Emergency and Remedial Response Plan. (2020). *Attachment F: Emergency and Remedial Response Plan 40 CFR 146.94(A) Clean energy Systems Mendota.*

Schlumberger, Attachment G: Construction Details Clean Energy Systems Mendota. (2020). *Attachment G: Construction Details Clean Energy Systems Mendota.*

Schlumberger, Attachment H: Financial Assurance Demonstration. (2020). *Attachment H: Financial Assurance Demonstration 40 CFR 146.85 Clean Energy Systems Mendota.*

Schlumberger, Class VI Permit Application Narrative. (2020). *Class VI Permit Application Narrative 40 CFR 146.82(A) Clean Energy Systems Mendota.*

SEI. (2019). Seismic Exchange Inc.

Suchsland, R. J. (1997). *Exploration and Development of the Blewett Trend, Northern San Joaquin Basin, California.* AAPG Pacific Section.

TGS. (2019). TGS-NOPEC Geophysical Company ASA.

USGS. (1983). *The Coalinga, California, Earthquake of May 2, 1983.* USGS. Retrieved from https://pubs.usgs.gov/pp/1487/report.pdf

USGS. (2003). In *Petroleum Systems and Geologic Assessment of Oil and Gas in the San Joaquin.*

USGS. (2005). *National Assessment of Oil and Gas Project - San Joaquin Basin Province (010) Boundary*. (C. R. Team, Producer) Retrieved from https://catalog.data.gov/dataset/national-assessment-of-oil-and-gas-project-san-joaquin-basin-province-010-boundary

USGS. (2019). *Earthquake Hazards Program*. Retrieved from https://earthquake.usgs.gov/

USGS. (2019). *U.S. Quarternary Faults*. Retrieved from USGS Geologic Hazard Science Center: https://usgs.maps.arcgis.com/apps/webappviewer/index.html?id=5a6038b3a1684561a9b0aadf88412fcf

USGS. (2019). *USGS Mineral Resources*. Retrieved from https://mrdata.usgs.gov/geology/state/state.php?state=CA

Vernik, L. a. (1989). Effects of rock elastic and strength properties in estimation of the state of stress at depth. *ISRM International Symposium*.

Winters, W. W. (1987). Roller bit model with rock ductility and cone offset. *SPE*.

Yielding. (2002). Shale Gouge Ratio - calibration by geohistory. *Norwegian Petroluem Society Special Publications*, 1-15.

Yielding, e. a. (1997). Quantitative Fault Seal Prediction. *AAPG*, 897-917.

Zoback, M. B. (2003). Determination of stress orientation and magnitude in deep wells. *International Journal of Rock Mechanics and Mining Sciences*, 1049-1076.